3D chiral metamaterial modular design with highly-tunable tension-twisting properties

Weiyun Xu [a], Zhao Liu [b, *], Liwei Wang [a], Ping Zhu [a, *]

[a] *The State Key Laboratory of Mechanical System and Vibration, School of Mechanical Engineering, Shanghai Jiao Tong University, Shanghai 200240, China*
[b] *School of Design, Shanghai Jiao Tong University, Shanghai 200240, China*

ABSTRACT

Chiral mechanical metamaterials are featured by their strong chiral effect induced by the node rotation and ligament bending deformation of chiral geometries. Despite their good compression-twisting performance in single principal direction, existing 3D chiral metamaterial designs are restricted to isotropic mechanical properties due to the geometry constraints imposed on the parametric model. In this study, a modular design method of 3D chiral metamaterials is proposed. By dividing the unit cell into several independent design units, this method greatly increases the design freedom and makes it possible to tailor properties in three principal directions. An effective and efficient articulated multi-link mechanism model is developed to study the deformation mechanisms of the proposed metamaterial under both normal and shear loadings. Through both analytical micropolar homogenization and finite element simulations, we demonstrate that the proposed 3D chiral metamaterial exhibits highly tunable tension-twisting properties, which is not achievable with existing designs. With better adaptability and application prospects, it provides inspiration for the 3D chiral metamaterial design with special functionalities, such as energy-absorbing materials and dynamic cloaks.

1. Introduction

Mechanical metamaterials are artificial materials engineered to achieve unprecedented mechanical properties that are not observed or unachievable in conventional materials, such as ultra-stiff [1], ultra-strong [2,3], ultra-light [1,3], reusable mechanical shock-absorbing [4, 5], bistable materials [6,7], negative Poisson's ratio [8,9], compression-twist coupling [10], and extraordinary resilience [3,11]. They enjoy a high tunability of properties with an immense design space of unit-cell microstructures and their tilling patterns. Capitalizing on the recent advances of manufacturing techniques, especially additive manufacturing (AM), it is now possible to manufacture these highly tunable metamaterials with complicated microstructures, opening up new avenues for the design of multifunctional structures [12–15].

Among various mechanical metamaterials, chiral mechanical metamaterials are a unique branch that exhibits strong chiral effects [16, 17]. Chirality, first introduced by Sir William Thomson, is used to describe an object that cannot overlap with its mirror image by rotations and translations alone [18]. Compression of the chiral mechanical metamaterials induces shearing and twisting responses in 2D [19,20] and 3D cases [21,22], respectively, known as chiral effect or compres-

sion-twisting effect. Such compression-induced-twisting (CIT) behaviors contribute to several successful industrial applications of chiral mechanical metamaterials, e.g., shape memorial smart deployable antenna and reconfigurable structures [23], mechanical adjustable stent [24], and phase transforming structures with shape switching abilities [25].

Considerable progress has been made in constructing the relation between unit-cell geometry and macroscale properties of three-dimensional (3D) chiral mechanical metamaterials, with an aim to understand the underlying mechanisms of chiral behaviors and guide rational designs. Generalized continuum mechanics theories, such as Cosserat's (micropolar) theory [26,27], are among the most commonly-used methods to study geometry-property relations. Utilizing micropolar theory, Frenzel et al. [28] related the geometrical parameters of 3D chiral mechanical metamaterials to its micropolar effective-medium constants with twist degrees of freedom. Kadic et al. [29] further studied static chiral Willis continuum mechanics of chiral metamaterials, and revealed that only one additional parameter directly influences chiral effects of homogeneous materials with cubic symmetry. And to extend the micropolar theory for 3D cubic chiral structure, a parameterized cubic-symmetry chiral unit cell is proposed based on a homogenization method to provide analytical relations between the structure

parameters and elastic constants of the chiral metamaterial [30]. Besides analytical homogenization-based methods, simulation-based methods are also adopted in studying the chiral behavior and underlying mechanisms of metamatarial unit cells [10]. The key insight obtained from these studies is that the realization of chiral behaviors relies on some special geometrical features that allow node rotation and ligament bending deformation [10,17,31]. However, existing chiral behavior analysis mainly focuses on axial compression/tensile, while the shear situation is rarely mentioned in the literature. More comprehensive exploration is needed in unraveling the relation between geometrical features and chiral effects.

Based on the insight obtained from the studies on geometry-property relations, various unit-cell microstructrues of 3D chiral metamaterials have been proposed [28,32,33]. The simplest type of parametric 3D chiral metamaterials has a Z-shape geometry and ligaments that are bend-dominant during deformation [30,34], commonly known as 3D Z-structure. It has good compression-twisting performance because it has fewer constraints from the other principal directions compared with those configurations with CIT features in three principal directions or in two directions. However, unit cells with a single Z-structure only exhibit chiral effects for axial compression/tensile at a specific direction and bring inconvenience in connecting different unit cells in other directions. To address this issue, attempts have been made to extend this design to achieve chiral effects in multiple directions. For example, by allocating Z-structures in three principal directions of a cube, Ha et al. [35] proposed a 3D chiral cubic lattice that successfully extends chirality from one direction to three principal directions, albeit with significant size effects, i.e., the compression-twisting effect decays dramatically as scaling factor (the ratio of macro and micro dimensions) increases, as confirmed experimentally in [36]. Nevertheless, all these designs [10,21,30,35] are restricted to isotropic mechanical properties (e.g., compression-twisting behavior, stiffness, and Poisson's ratio) due to the geometry constraints imposed on the parametric model. One promising method to realize anisotropic properties is to utilize the concept of modular design, i.e., dividing the unit cell into several independent design units, to enable greater design freedom with decoupled property designs in different directions. Despite its promise, extending the modular design to 3D chiral metamaterials has not yet been well investigated. Recently, Huang et al. [37] took each of the eight vertices of the cube as a design unit and generated a 3D antitetrachiral structure with negative Poisson's ratio. Although each design unit is chiral, the constituent unit cell does not possess chirality. Moreover, there is still great potential for the tunability of the properties of chiral unit cells that are designed based on 3D Z-structures.

In this study, a novel 3D chiral metamaterial that enables modular design is proposed. The proposed chiral cubic unit cell is composed of six independent design units (noted as "1/6 structures" in this study) with separate geometrical design parameters, which is beneficial in tailoring the target anisotropic chiral properties and connecting unit cells with different geometries. An articulated multi-link mechanism model is used to provide insights into the deformation mechanisms of the proposed metamaterials under both normal and shear loadings. Through both analytical micropolar homogenization and finite element simulations, we demonstrate that this new 3D chiral metamaterial exhibits highly tunable tension-twisting properties, which is not achievable with existing designs. By the proposed method, it's promising to design more 3D chiral metamaterials with better adaptability and application prospects, such as energy-absorbing materials and dynamic cloaks.

2. Methodologies

In this section, we first propose a 3D chiral metamaterial with a simple but flexible modular design scheme. Homogenization considering the micropolar elastic behaviors is then adopted to study the relations between geometry parameters and micropolar elasticity. A continuum model is further developed to evaluate the mechanical properties of the proposed 3D chiral metamaterial.

2.1. Proposed geometry of chiral unit cell

The geometry of the proposed chiral lattice structure is illustrated in Fig. 1. To obtain a more flexible design and better connectivity among unit cells, modular design is applied in designing the chiral unit cell, i.e., the design domain of a single cell is partitioned into six independent regions (Figs. 1b and 1c). In each region, a chiral structure (noted
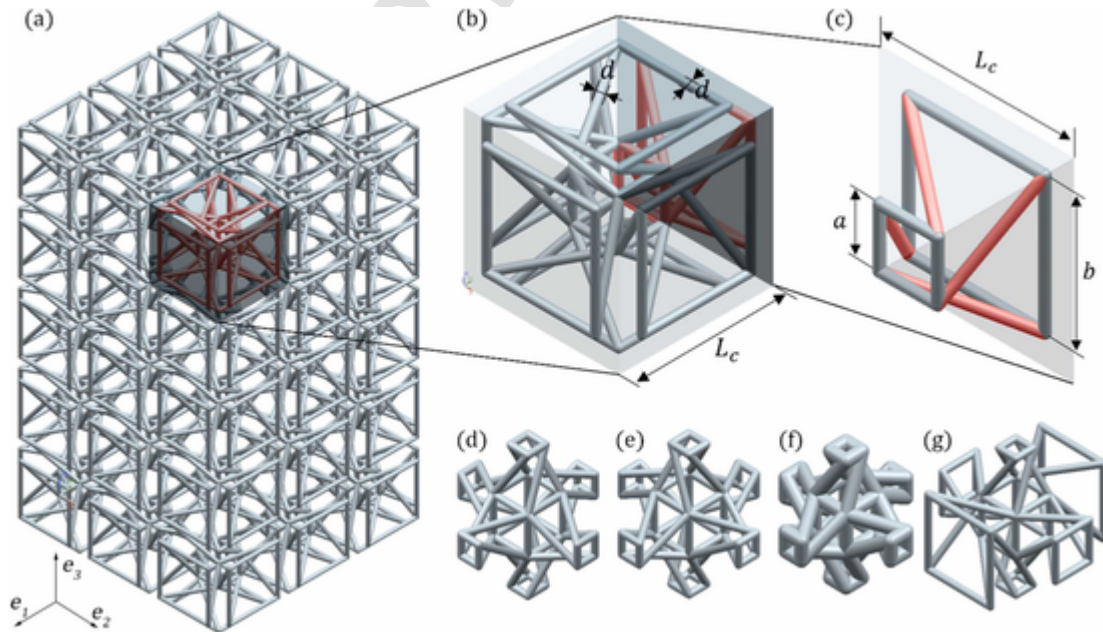
Fig. 1. Geometry of the proposed 3D chiral lattice. (a) chiral mechanical metamaterial constructed by chiral unit cells, (b) unit cell design domain partitioned into six design units, (c) 1/6 chiral structure composed of two squares linked by four ligaments. Variants of the structure in (b) are shown in (d)~(g) by (d) increasing v and decreasing ω, (e) changing rotation direction from right-handed to left-handed (all three principal directions), (f) increasing η, and (g) varying anisotropy arrangements in three principal directions.

as 1/6 chiral structure) is constructed by rods with different sizes as illustrated in Fig. 1b and Fig. 1c. Specifically, two square frames made of rods are connected clockwise or counterclockwise (front view from outside to inside) by four ligaments at four vertices, which induce left-handed and right-handed rotations, respectively. This 1/6 chiral structure is the minimal design unit to introduce chirality. The two square frames in 1/6 chiral structures can have different sizes, rendering higher tunability than the existing simple 3D Z-structure [10,21,30,35]. For example, the chiral unit cell proposed in [35] consists of cubes that are directly connected by four ligaments between them, while in the present design, those four straight ligaments break in the middle and are connected by a square frame. In this case, it enables the inclination of the ligaments to become larger by either adjusting the cubic length or the size of the frame, increasing the designability of the original 3D Z-structure. In addition, the topology of the chiral unit cell changes after adding the square frame, differentiating the proposed design from the existing ones.

Without losing generality, we use the same 1/6 chiral structures for all the six partitioned regions in this study, which makes the unit cell cubic-symmetric, to facilitate the demonstration of the feasibility and characteristics of the proposed structure. In this case, four geometry parameters are adequate to describe the configuration of a chiral unit cell, i.e., prism length of the unit cell L_c, prism length of the inner cube a, side length of the outer square frame b, and diameter of the rob d. With L_c fixed, the remaining parameters can be converted to dimensionless parameters as:

$$\nu = a/L_c, \quad \omega = b/L_c, \quad \eta = d/L_c, \tag{1}$$

with value range

$$0 < \nu < 1, \quad 0 < \omega < 1, \quad 0 < \eta < 1.$$

To enable linkage between rods without interference, geometry constraints should be considered that the side lengths of inner square frames must be the same dimensions as the connected structure. With these, the detailed geometry of a chiral unit cell can be denoted as (L_c, ν, ω, η). It is noted that the rotation direction of chiral structure should be declared additionally, and right-handed chiral unit cell is used in this study.

The proposed chiral unit cell contains more design parameters, and thus enable a wider variation in sizes and higher diversity in shapes than the previous 3D Z-structure in the literature [10,21,30,35]. In addition, the unit-cell modular design allows the structure to exhibit chirality in each of the three principal directions. Other mechanical properties (Poisson's ratio, stiffness, *etc.)* can also be designed independently in three directions by changing the diameter, length and rotation direction (left-handed or right-handed) of the rod structure. Moreover, the outer square frames help to improve the connectivity between unit cells by imposing simple constraints on the ligaments.

2.2. Continuum model of micropolar elasticity

In order to establish the relationship between the geometric parameters and the mechanical properties, a homogenization method for the proposed 3D chiral metamaterial is developed based on micropolar theory. As a special microcontinuum theory [27], the micropolar theory assumes that each point of the continuum has six degrees of freedom, i.e., displacement u_i and microrotation ϕ_i in three directions, with $i \in \{1, 2, 3\}$ representing the axis. Accordingly, the micropolar strain ϵ_{ij} and curvature k_{ij} are given as

$$\epsilon_{ij} = \varepsilon_{ij} + e_{ijk}(r_k - \phi_k) = u_{j,i} + e_{jik}\phi_k,$$
$$k_{ij} = \phi_{i,j}, \tag{2}$$

where e_{ijk} is the permutation symbol, and $r_k = \frac{1}{2}e_{klm}u_{m,l}$ is the macro-rotation vector. Herein, the usual Einstein summation convention is used, with the comma denoting partial differentiation with respect to a corresponding coordinate. To consider the effect of noncentrosymmetry in a micropolar elastic solid, three extra elastic constants B_1, B_2 and B_3 [38] are introduced into those of isotropic micropolar solid in predicting the torsional deformation of acentric micropolar solid under compression. Thus, the strain energy density of a linear elastic micropolar solid without initial stress and initial couple stress can be obtained from strain and curvature tensors as

$$w = \frac{1}{2}\epsilon_{ij}A_{ijkl}\epsilon_{kl} + \epsilon_{ij}B_{ijkl}k_{kl} + \frac{1}{2}k_{ij}C_{ijkl}k_{kl}, \tag{3}$$

where A, B and C are rank four elastic tensors. As a result, the stress σ_{ij} (force per unit area) and coupled stress m_{ij} (torque per unit area) are derived as

$$\sigma_{ij} = \partial w/\partial \epsilon_{ij} = A_{ijkl}\epsilon_{ij} + B_{ijkl}k_{kl},$$
$$m_{ij} = \partial w/\partial k_{ij} = B_{ijkl}\epsilon_{ij} + C_{ijkl}k_{kl}, \tag{4}$$

They are the constitutive equations for linear isotropic Cosserat elasticity. It should be noted that both micropolar strain and stress are asymmetric with the resulting moment balanced by the coupled stress.

The specialty of the proposed chiral lattice lies in its combination of cubic symmetry and noncentrosymmetry. Following the method in [30] (see Appendix A for the derivation in detail), elastic tensors can be obtained based on the energy equivalence principle by

$$A_{ijkl} = \partial^2 w/\partial\epsilon_{ij}\partial\epsilon_{kl}, \quad B_{ijkl}$$
$$= \partial^2 w/\partial\epsilon_{ij}\partial k_{kl}, C_{ijkl}$$
$$= \partial^2 w/\partial k_{ij}\partial k_{kl}, \tag{5}$$

where w is the strain energy density of unit cell. The relationship between strain energy of 1/6 chiral structure $W_{1/6}$ and w can be given as

$$w = W_{UC}/V_{UC} = 6W_{1/6}/L_c^3, \tag{6}$$

There are 12 elastic constants: λ, G, κ, C_a; B_1, B_2, B_3, C_b; and α, β, γ, C_c. λ and G are the *Lamé constants*, α, β, γ and κ are micropolar elastic constants, B_1, B_2 and B_3 are elastic constants associated with chirality (noncentrosymmetry), and C_a, C_b and C_c are elastic constants characterizing cubic symmetry.

According to Eq. (5) and Eq. (6), the key step to derive the 12 elastic constants with the aforementioned geometry parameters is to get the strain energy of the chiral unit cell. Analytically, the inner cube and the outer squares of the chiral lattice are assumed to be rigid, and the 4 ligaments in 1/6 chiral structure are assumed to be the only part to store strain energy during deformation (the assumption is commonly used in chiral structure analysis [30,35] and can be justified in later FE analysis). In the process of strain energy calculation, since the deformation of a ligament is bend-dominant [19], the ligaments are assumed to be Euler-Bernoulli beams considering shear correction under the linear elastic small deformation assumption.

As shown in Fig. 2a, the positions of the vertices are marked as R^m and O^m before deformation and $\widetilde{R^m}$ and $\widetilde{O^m}$ after deformation ($m = 1, 2, 3, 4$), and O is the origin of the coordinate system. Thus, the location vector of each ligament in a 1/6 chiral structure before and after deformation can be denoted as $\boldsymbol{T^m} = \begin{bmatrix} OR^m & OO^m \end{bmatrix}^T$ and $\widetilde{\boldsymbol{T^m}} = \begin{bmatrix} O\widetilde{R^m} & O\widetilde{O^m} \end{bmatrix}^T$ respectively ($m = 1, 2, 3, 4$). Accordingly, its strain energy is given as

$$W_{1/6} = \frac{1}{2}\left(\widetilde{\boldsymbol{T^m}} - \boldsymbol{T^m}\right)^T \boldsymbol{K}\left(\widetilde{\boldsymbol{T^m}} - \boldsymbol{T^m}\right), \tag{7}$$
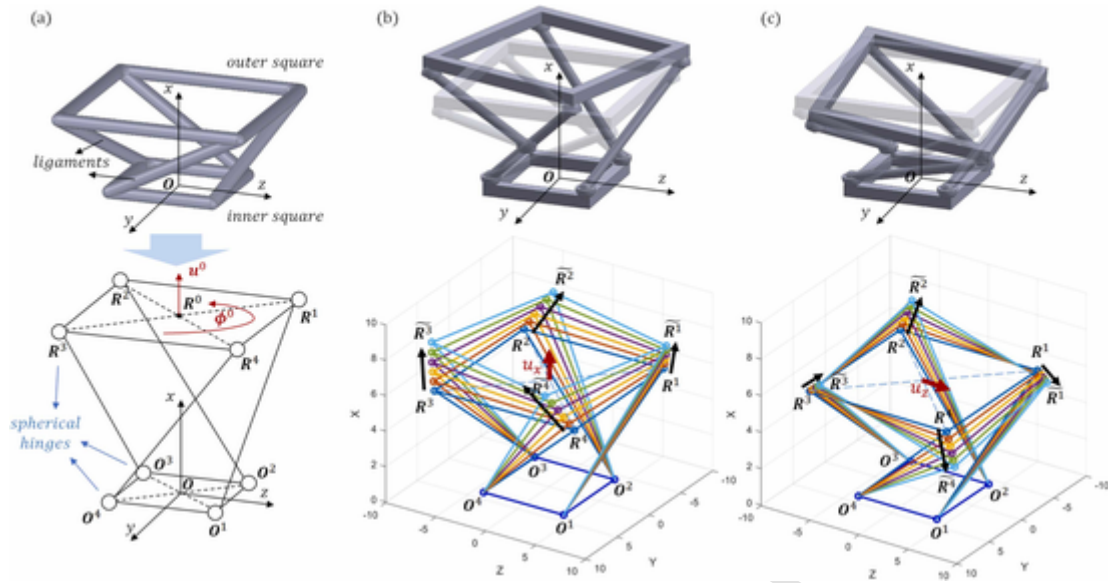
Fig. 2. Calculation of DOFs and deformation mechanism of 1/6 chiral structure. (a) 1/6 chiral structure modeled as an articulated multi-link mechanism under boundary conditions $(\boldsymbol{u^0}, \boldsymbol{\phi^0})$, where the inner square, outer square and ligaments are all rigid bodies connected by spherical hinges, and the inner square is fixed. (b) Model (top) and corresponding deformation process (bottom) with axial displacements u_x imposed to the center of the rigid outer square. (c) Model (top) and corresponding deformation process (bottom) with tangential displacements u_z imposed to the center of the rigid outer square. In (b) and (c), the transparent structures illustrate the mechanism before movements, and the black arrows show the tendency of deformations.

where $\boldsymbol{K}$ is the stiffness matrix of Euler-Bernoulli beam considering shear correction in the global coordinate system. Substituting Eq. (7) into Eq. (6), the strain energy density of unit cell can be obtained as

$$w = 3\left(\widetilde{\boldsymbol{T^m}} - \boldsymbol{T^m}\right)^T \boldsymbol{K} \left(\widetilde{\boldsymbol{T^m}} - \boldsymbol{T^m}\right)/L_c{}^3, \tag{8}$$

Since the coordinates of each endpoint are directly related to the parameters of the chiral structure, the mathematical connection between the elastic constants $(\lambda, G, \kappa, C_a, B_1, B_2, B_3, C_b, \alpha, \beta, \gamma, C_c)$ and the geometry parameters (L_c, v, ω, η) can be established by substituting Eq. (8) into Eq. (5).

3. Results and discussion

In this section, the deformation mechanism of the proposed structure is studied. The relationship between the structural geometric parameters and the micropolar elastic constants is then demonstrated, which is further used for the twist angle prediction of the structure under axial compression. The results are compared with those of a finite element model, illustrating the superior performance of the present 3D chiral metamaterial. In addition, in order to investigate the size effect of the material tension-twisting properties, structures with different size scale factors are constructed and also compared laterally with a similar structure in the literature.

3.1. Deformation mechanism

The traditional analysis of deformation mechanisms is based on the kinematic analysis of the structure [10]. To obtain accurate predictions through this method, precise definitions of the boundary conditions of the system and the intrinsic properties of the material are required, which are difficult to calculate or time-consuming. However, in this study, it is sufficient to obtain the displacements of each part of the structure under deformation. On the one hand, force analysis is no longer necessary because the deformation mechanism can be illustrated by showing the tendency of displacements of 1/6 chiral structure when it is constrained by the displacement boundary conditions; on the other hand, due to the assumption of small deformation, linear elasticity, and

rigidity of the two squares in 1/6 chiral structure, the displacements of the ligaments can be directly used to obtain the strain energy under the beam assumption.

Specifically, the 1/6 chiral structure is modeled as an articulated multi-link mechanism which is commonly used in robotics [39,40]. The four ligaments are separately connected with the outer square and the inner square by spherical hinges (Fig. 2a). The displacement at both ends of the ligaments $\left(\widetilde{\boldsymbol{T^m}} - \boldsymbol{T^m}\right)$ can be obtained from the transition and rotation at the center point of the rigid outer square. This placement is plugged into Eq. (8) to calculate the strain energy (see Appendix B for more detailed derivations). As a result, the rotation vector of the center point of the rigid outer square $\boldsymbol{\phi^0}$ can be calculated by given displacement $\boldsymbol{u^0}$ and vice versa:

$$\boldsymbol{\phi^0}\left(\phi_x^0, \phi_y^0, \phi_z^0\right) = f\left[\boldsymbol{u^0}\left(u_x^0, u_y^0, u_z^0\right)\right]. \tag{9}$$

It should be noted that although the displacement and rotation of the structure are obtained under the assumption that all parts of the mechanism are rigid, the strain energy calculated analytically is consistent with that obtained from the numerical simulation. Two different boundary conditions, i.e., axial displacement $u_x = u_x^0$ and tangential displacement $u_z = u_z^0$, are imposed to the center point of the rigid outer square. The corresponding deformation process for these two boundary conditions is shown in Fig. 2b and c, respectively. Taking the right-handed 1/6 chiral structure in Fig. 2b as an example, when the outer square undergoes an axial positive displacement u_x, the end of the ligament attached to the square R^m tends to move along the positive direction (x-axis), while the other end of the ligament O^m attached to the inner square is fixed. Since the projections of O^m and R^m in the transverse direction do not overlap, the two points tend to approach each other in the transverse direction (y-axis or z-axis), which leads to the bending movement of the ligament toward the oblique top. As a result, the tendency to bend in the four ligaments drives the outer square $R^1 R^2 R^3 R^4$ to rotate right-handedly and to displace in the axial direction (x-axis). As for the tangential case (shear situation) in Fig. 2c, the causes of ligament movement are similar to the axial one described above. However, it is interesting to observe different responses of the four ligaments to the same tangential displacement constraint, which makes the overall

movement of the outer square differ from the tensile situation. The difference in the magnitude and direction of the bending motion depends on the relative position relationship between the spatial position of the ligament and the applied displacement constraint. To be specific, as is shown in Fig. 2c, O^2R^2 ligament tends to bend downward diagonally, while O^4R^4 ligament tends to bend upward diagonally. And O^1R^1 and O^3R^3 ligaments undergo a relatively small lateral bending movement. This causes the outer square to tilt under the tangential displacement constraint: a significant rotation along the R^1R^3 direction.

It is worth pointing out that, the solution of the 1/6 chiral structure articulated multi-link mechanism model is unique, i.e., given any component of the rotational and translational degrees of freedom, the postures of other components can be uniquely determined accordingly. Moreover, when $u_x = u_z$, the response of the chiral structure to the tangential displacement constraint is greater than that to the axial displacement constraint, indicating a bending deformation behavior dominant over a stretching one in response to given boundary constraints. Through the modeling, the deformation mechanism of the 3D Z-shaped chiral structure (Z-structure) is illustrated under not only axial load but also tangential load. It indicates that the twist behavior of the chiral structure is related to bend-dominant deformation of the ligaments, which is consistent with the findings of the literature [10].

3.2. Micropolar elastic constants of 3D Chiral metamaterial

Twelve elastic constants of the micropolar elasticity analytically obtained by the energy-based homogenization method (*Section 2*) are illustrated in Fig. 3. As a comparison for accuracy, the results of the fine finite element model (FEM) of the chiral unit cell are illustrated as well. In the FEM which is analyzed by Abaqus Standard solver, all rods of the chiral unit cell (Fig. 1b) are set as B31 beam elements with fine mesh and periodic boundary conditions and geometric nonlinearity are considered (refer to **Appendix B** for details of the calculation procedure).

Constants in tensor A_{ijkl}, B_{ijkl} and C_{ijkl} are normalized as $(\lambda, G, \kappa, C_a)/E_0$, $(B_1, B_2, B_3, C_b)/E_0L_c$ and $(\alpha, \beta, \gamma, C_c)/E_0L_c^2$, respectively, to unify the magnitudes for a better illustration. Herein, E_0 stands for the elastic modulus of the constituent material. As shown in Fig. 3, results of the continuum model (CM) derived from the homogenization method match well with those from numerical simulations (FEM). The monotonicity of the constants varies. The fact that a consistent increase or decrease with v or ω does not occur is because the two parameters together define the spatial configuration of 1/6 chiral structure, which in turn affects the mechanical properties. Furthermore, invariance of the elastic constants in *A*, *B* and *C* exists with respect to strain ε within linear elastic range. Equivalence relations among the constants can thus be derived by the calculated results as

$$\lambda = C_a,$$
$$B_1 = B_2 = C_b,$$
$$\alpha = \gamma = C_c. \tag{10}$$

From Fig. 3, it can be noted that the four geometry parameters (L_c, v, ω, η) form a large parametric design space that allows diverse geometries and highly tunable mechanical properties of the chiral unit cell. For example, the maximum shear modulus G is over 5 times larger as the minimum one. And the first *Lamé Constant* λ can be tuned from positive to negative values, so as α, γ, κ. The variation patterns of the 12 micropolar elastic constants work as indicators of the parametric distribution of the elastic and chiral properties of the chiral metamaterial.

By defining

$$E = \lambda + 2G + 2C_a,$$

$$\phi^2 = \frac{(B_1 + 2B_2 + 2C_b)^2}{(\lambda + 2G + 2C_a)(\alpha + 2\beta + 2C_c)},$$
$$l_c^2 = \frac{\beta + \gamma - C_c}{2(\lambda + 2G + 2C_a)}, \tag{11}$$

the elastic-static mechanical behavior of the proposed 3D chiral metamaterial is further discussed, as is shown in Fig. 4. In Eq. (11), E is the Young's modulus in principal direction, ϕ is the characterization length measuring the strength of the noncentrosymmetric coupling [38], and l_c is the characterization length determining the magnitude of couple stress [41,42].

To facilitate the visualization of modulus with different scales, the vertical coordinates in Figs. 4a-4d are expressed in logarithmic coordinates. It can be observed from Figs. 4a and 4b that with L_c and η fixed, specific tensile module is bigger at small v or ω than a bigger one. Small v or ω reduces the effect of bending-domination during deformation, obtaining high stiffness at the expense of weakening the chiral effect. When $v = 0$ or $\omega = 0$, the chiral structure becomes achiral. And there exists a sudden increase of specific tensile module and specific shear module as ω reaches zero, which is indicated by dashed lines in Figs. 4b and 4d.

From Figs. 4e and 4f, it can be demonstrated that ϕ, which characterizes the decay rate of E and is related to coupling tensor B_{ijkl}, varies greatly for different values of v. And it shows a more drastic increase at small ω, which indicates a greater change of compression-induced-twisting (CIT) behaviors. As for the characterization length l_c, it can be viewed as the indicator of size effect, which is comparable in size to unit cell [41,43]. Results in Figs. 4g and 4h show that l_c is sensitive at large v and is linearly related to ω, suggesting that the bigger v or ω is (a relatively bigger 1/6 chiral structure in size), the more obvious the size effect is. On the other hand, as v or ω approaches zero, the unit cell becomes achiral and l_c diminishes as 0, reducing the micropolar elasticity into a classical Cauchy elasticity.

3.3. Mechanical behaviors of 3D chiral metamaterial

In this section, the continuum model (CM) is further applied to predict the mechanical response of macro structures assembled by the chiral unit cell. Compared with time-consuming FE analysis, CM is more efficient and can derive analytical solutions directly by solving the partial differential equation. Different levels of chiral effect are observed by adjusting geometry parameters, and advantages over the benchmark 3D chiral metamaterials are confirmed. And results match well with those of fine FE models (FEM).

3.3.1. Tension-twisting properties of chiral macrostructure

As a demonstrative case study of the proposed 3D chiral metamaterial, rectangular chiral structures are constructed by periodic arrangement of the chiral unit cell, denoted as $N_1 \times N_2 \times N_3$ to indicate the number of unit cells arranged in the three main directions. Here a $5 \times 10 \times 5$ rectangular chiral structure is used to test the tension-twisting properties. Defining scale factor as

$$N = L_c/L_s, \tag{12}$$

then in this case the scale factor $N = 5$. Boundary conditions with fixed displacement constraints in the axial direction are applied (as demonstrated in Fig. 5a), and twist capability of the macrostructure is measured by rotation angle per axial strain θ/ε. Predictive results of the continuum model are obtained through COMSOL Multiphysics (COMSOL, Inc.) [28], while finite element models are calculated by Abaqus Standard solver.

Given $L_c = 10$, the distribution of tension-twisting properties of the structure with geometry parameters (v, ω, η) under a fixed axial strain
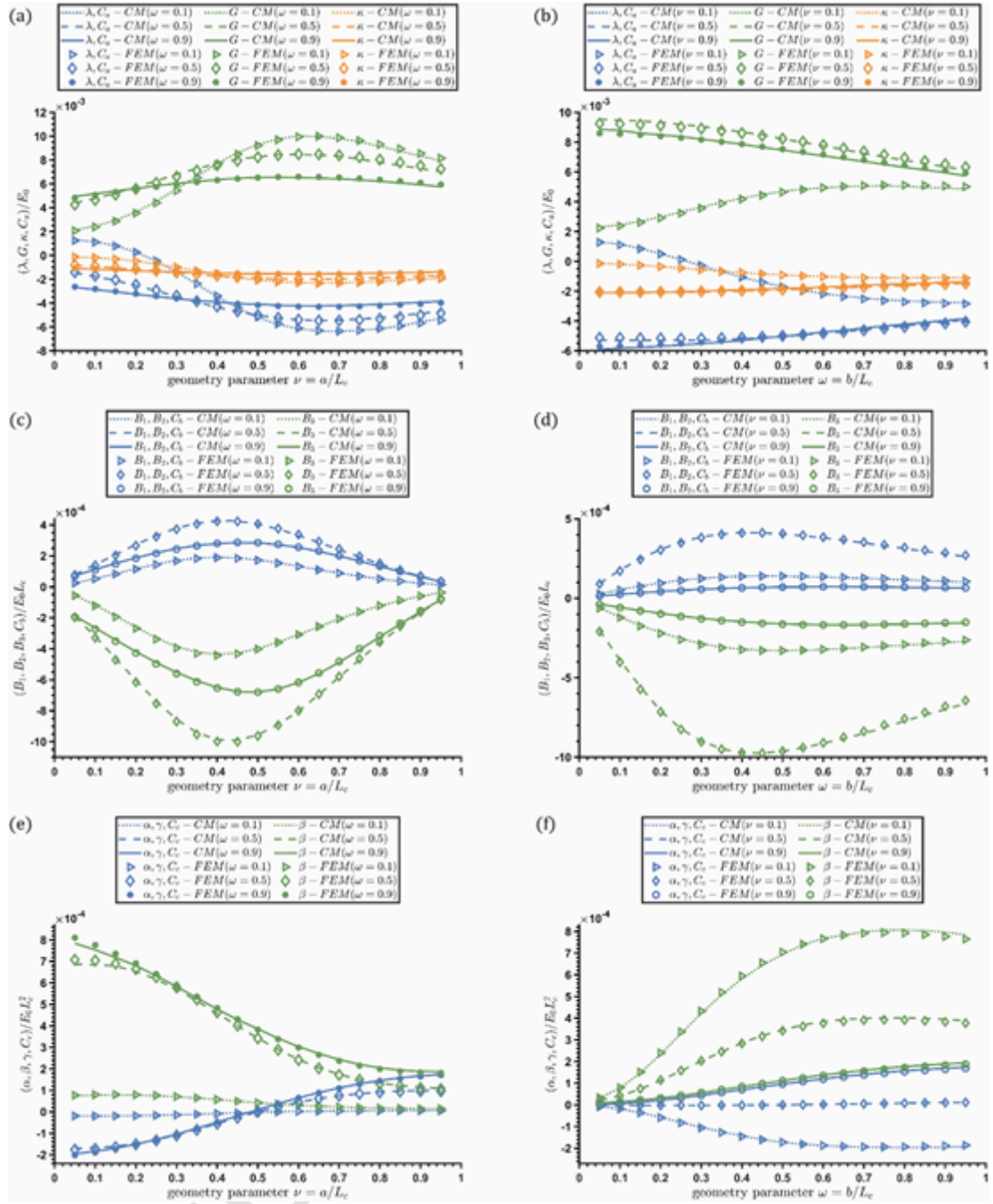
Fig. 3. Micropolar elastic constants versus parameters ν and ω. (a), (c) and (e) respectively stand for $(\lambda, G, \kappa, C_a)$ in tensor $\boldsymbol{A}$, (B_1, B_2, B_3, C_b) in tensor $\boldsymbol{B}$ and $(\alpha, \beta, \gamma, C_c)$ in tensor $\boldsymbol{C}$ versus ν, for various ω. (b), (d) and (f) respectively stand for $(\lambda, G, \kappa, C_a)$, (B_1, B_2, B_3, C_b) and $(\alpha, \beta, \gamma, C_c)$ versus ω, for various ν. $L_c = 10, \eta = 0.05$ in this case.

($\varepsilon = 0.01$) is shown in Fig. 5. It can be demonstrated that the thicker the ligament (the larger η), the smaller the angle of twist. Due to the linear elasticity assumption adopted in CM, there exists a small but acceptable discrepancy between the twisting angle predicted from CM and those from FEM, especially at small η. Moreover, the twist angle reaches the maximum when ν ranges between 0.15 and 0.25 as shown in Fig. 5c, but then decays dramatically as ν increases. To explain this phenomenon, for a given ω, a smaller ν implies a smaller inner cube with a smaller radius of rotation, and thus the 1/6 chiral structure requires a larger angle of rotation to keep up with an equivalent axial displacement. Since the bending deformation of the ligament is large at this point, the nonlinearity makes the prediction error of CM larger. How-

ever, as ν continues to get smaller to a scale comparable to η, the geometric features of chirality tend to be negligible and the stretching deformation of ligaments, instead of the bending deformation, will become dominant, resulting in a decrease in the twisting angle of the structure. As a $50mm \times 100mm \times 50mm$ sample, twist per axial strain exceeding $18°/\%$ is measured at $\nu = 0.15, \omega = 0.9, \eta = 0.025$, which is much greater than that of the chiral metamaterial proposed by Fenzel [28] on overall millimeter-sized samples ($2°/\%$).

According to the results, large ω and small ν together determine an effective 1/6 chiral structure with large twist under tensile load, while relatively small ν and big ω make few contributions to the tension-twisting properties. As shown in Fig. 4 and Fig. 5, ν is the dominant fac-
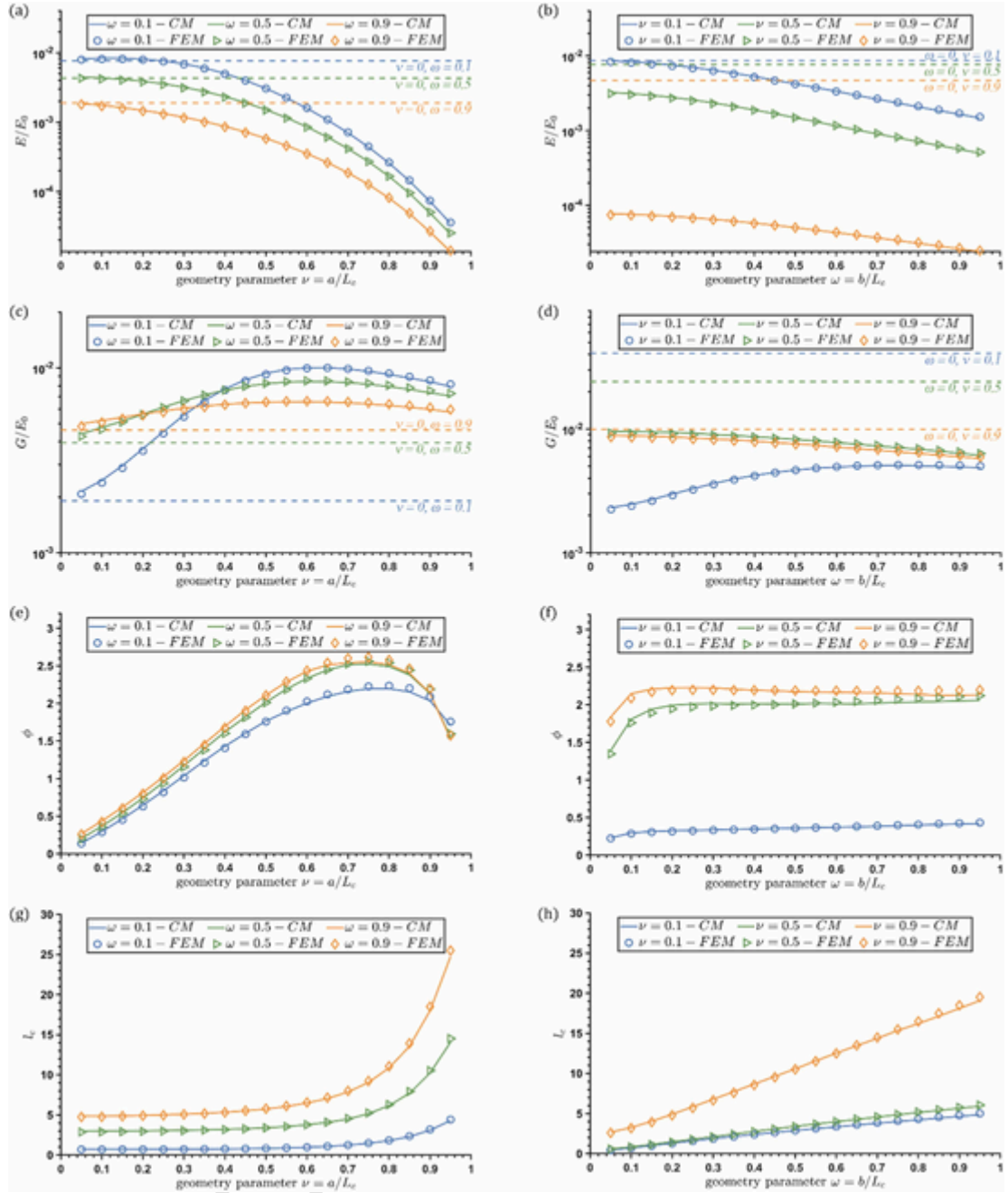
Fig. 4. Mechanical properties of the proposed 3D chiral metamaterial. (a) and (b): Specific Young's modulus E/E_0 versus v and ω respectively. Dash lines represent for achiral situations. (c) and (d): Specific shear modulus G/E_0 versus v and ω respectively. Dash lines represent for achiral situations. (e) and (f): characterization length ϕ versus v and ω respectively. (g) and (h): characterization length l_c versus v and ω respectively. $L_c = 10, \eta = 0.05$ in this case.

tor in controlling the chiral effect of the proposed chiral metamaterial. This suggests that the size of the inner cube in a chiral unit cell is critical in deciding its twisting capability. And it is worth noting that the Poisson's ratio remains zero for all different sets of parameters. It can be concluded from the results that the modular design expands the property range of chiral metamaterial by introducing more parameters. Targeted tension-twisting properties along with different tensile and shear modulus can be obtained by designing various chiral structural families.

3.3.2. Size effect of 3D chiral metamaterial

Existing 3D chiral metamaterial designs based on Z-structure show obvious size effects [10,21,30,35]. As indicated in [28], the metamater-

ial unit cell with Z-structure yields large twist angles per axial strain when $N = 1$ but decreases fast when N goes from 1 to 5. In order to demonstrate the advantages of the proposed chiral metamaterial, a comparison of twist angles per axial strain between chiral metamaterial based on Z-structures and our new 3D chiral metamaterial is carried out in this section.

Specifically, the chiral lattice proposed in [30], which is a classical Z-structure-based chiral design, is selected as the benchmark. This unit cell consists of circular rings in the center and ligaments outside, where the rings were taken as rigid and the ligaments were assumed to be Euler-Bernoulli beams for analysis. For a fair comparison, the same volume fraction is assigned to both types of unit cells. Provided that the length of unit cell L_c and the diameter of the rod structures d remain
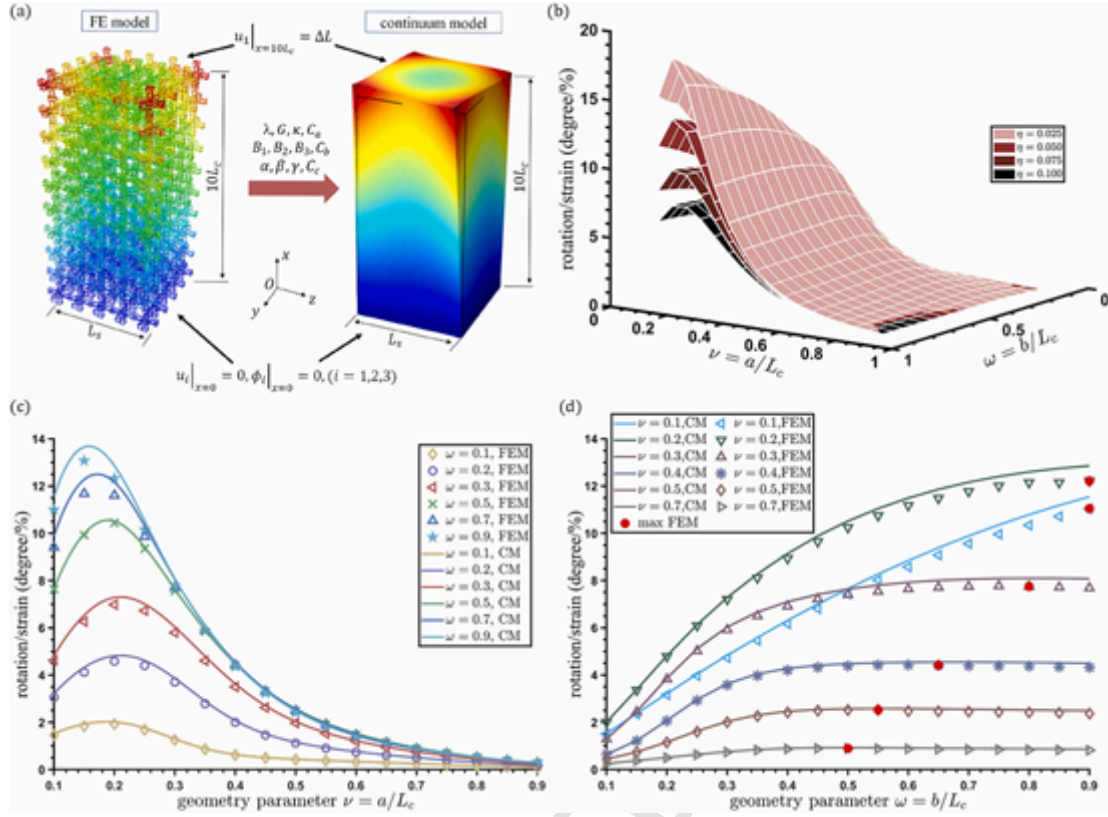
Fig. 5. Relationship between twist capacity of $5 \times 10 \times 5$ chiral macrostructure and the three geometry parameters. (a) The finite element model (FEM) and continuum model (CM) of the 3D chiral structure. (b) Twist property space with respect to ν, ω, and η. (c) Rotation angle per axial strain with respect to ν. (d) Rotation angle per axial strain with respect to ω. Maximum rotation values calculated by FEM are colored in red for different levels of ν.

unchanged, the total length of the rod structures l_{UC} within a single unit cell will be always equal to the benchmark one l_{UC}^b. Thus, we have

$$
\begin{aligned}
l_{UC} &= l_{inner}(\nu) + l_{outer}(\omega) + l_{ligament}(\nu, \omega) \\
&= l_{ring}^b + l_{ligament}^b \\
&= l_{UC}^b
\end{aligned}
\tag{13}
$$

By setting the parameters of the benchmark structure, the dimensionless parameters of the proposed chiral structure are determined. In this case, the dimensionless parameter associated with the rings of the benchmark structure is set to 0.2. Eq. (13) yields a quadratic equation with respect to ν and ω. Given any ν in the range of values, the corresponding ω is obtained (non-positive solutions are excluded). Therefore, $\nu = 0.1, \omega = 0.23; \nu = 0.2, \omega = 0.2; \nu = 0.3, \omega = 0.15$ are all reasonable sets of parameters that make the volume fractions the same, which will be used in the analysis for the comparison of torsional performance with the benchmark chiral metamaterial, as demonstrated in Fig. 6.

As illustrated in Fig. 6a, the proposed chiral metamaterial and the benchmark show a similar decaying trend as N increases, which is due to the similarity in the chiral topology. However, under the same scale factor, the proposed chiral metamaterial has greater rotation angles per axial strain than the benchmark. In this case, it has an improvement as large as 80% over the benchmark chiral metamaterial when $N = 1$ under the optimal sets $\nu = 0.2, \omega = 0.2$. This demonstrates an even better chiral effect of the proposed 3D chiral metamaterial than the existing ones which are based on Z-structures. It can be observed from Fig. 6b that the twist angle decreases greatly as the scale factor increases, indicating a shift in material properties from micropolar to Cauchy elasticity. But the decay rate is less than the benchmark structure in Fig. 6a. Furthermore, the tensile modulus is marked directly beside the unit cells in Fig. 6c-f, which does not exhibit any size effects. It can be concluded that, compared with the benchmark structure, the macrostruc-

ture arranged by the proposed chiral unit cell has higher twist capacity along with higher compliance. Although this may not be desirable in load-bearing situations, it is appropriate in specific application scenarios, such as flexible functional structures.

4. Conclusions

In this paper, we propose a novel 3D chiral metamaterial that highlights the concept of modular design, providing higher design freedom than existing designs. With the modular design method, mechanical properties (e.g., compression-twisting, stiffness, Poisson's ratio) can be tailored independently in three directions to achieve anisotropic properties, without violating geometry and connectivity constraints. The underlying deformation mechanism of each 1/6 chiral structure in the proposed design is unraveled with an articulated multi-link mechanism model, by which the translation and rotation degrees of freedom under shearing deformation can be obtained effectively. Both micropolar homogenization method and finite element analysis are carried out to study the relationship between geometry parameters and the corresponding elastic constants. The results show that the proposed chiral metamaterial exhibits highly-tunable twist capability along with vast coverage of mechanical properties, validating the effectiveness of the proposed design. Moreover, through a comparative study with an existing chiral design, we demonstrate that our proposed 3D chiral metamaterial greatly improves the compression/tensile-twist performance under the same volume fraction constraint. Size effects are investigated and compared with benchmark chiral metamatarial. It shows that the proposed chiral metamaterial exhibits better twist performance under the same scale factor.

Based on the results, it can be concluded that the concept of modular design in chiral unit cells can greatly increase the design freedom, and thus makes it more flexible in tailoring chiral properties. It is
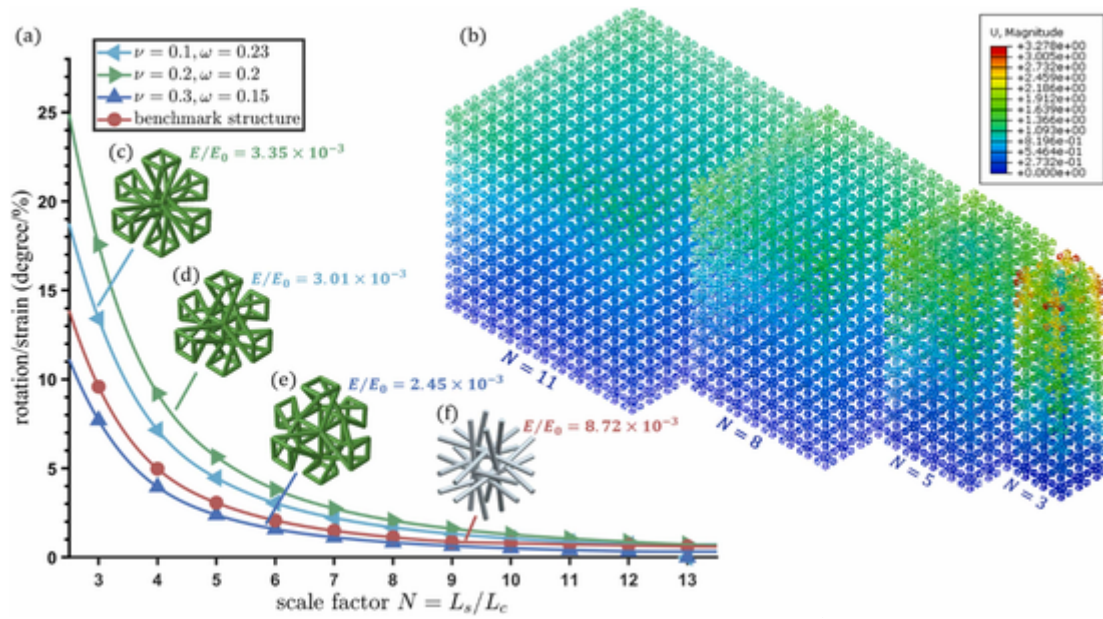
Fig. 6. (a) Comparison of the decay of twist capability between proposed 3D chiral metamaterial and benchmark chiral structure with respect to scale factor. (c), (d), and (e) Different chiral unit cells which have the same volume fraction with the benchmark chiral unit cell [30] in (f). Each specific tensile modulus is marked. (b) Size effect visualization shown by $N \times 10 \times N$ rectangular chiral structures under the same parameters $\nu = 0.2$, $\omega = 0.2$, and strain constraint $\varepsilon = 0.01$.

promising to include more structural families with different degrees of chirality in the three principal axis directions to achieve spatially varying properties for more complicated functionalities, such as energy-absorbing and vibration-damping structures with heterogeneous stiffness requirements.

CRediT authorship contribution statement

Weiyun Xu: Conceptualization, Methodology, Software, Validation. **Zhao Liu**: Data curation, Writing – original draft, preparation. **Liwei Wang**: Investigation, Writing – review & editing. **Ping zhu**: Supervision.

Declaration of Competing Interest

The authors declare that they have no known competing financial interests or personal relationships that could have appeared to influence the work reported in this paper.

Data availability

The data that support the findings of this study are available from the corresponding author upon reasonable request.

Appendix A.

This appendix presents in detail the derivation of the elastic tensors in constitutive equations. The specialty of the proposed chiral lattice lies in its combination of cubic symmetry and noncentrosymmetry. On the one hand, the cubic structure makes the elastic tensors invariant under $n\pi/2$ rotation along the coordinate axis direction. To be specific, B_{ijkl} and C_{ijkl} in Eq. (4) are pseudo tensors. It means these tensors change as the direction of microrotation vector ϕ_i inverses, as is suggested from Eq. (2). On the other hand, the chiral lattice doesn't have a center of symmetry, which is defined as noncentrosymmetry, and the invariance of strain energy under an inversion of specific axis no longer exists [38].

According to [43], elastic constitutive tensors of the cubic symmetry unit cell can be decomposed into an isotropic term D_{ijkl}^{iso} and a cubically symmetric term D_{ijkl}^{cubic} as

$$D_{ijkl} = D_{ijkl}^{iso} + D_{ijkl}^{cubic}, \tag{A.1}$$

where D_{ijkl} represents any elastic constitutive tensor A_{ijkl}, B_{ijkl}, or C_{ijkl}. The isotropic part can be written as

$$D_{ijkl}^{iso} = D_1 \delta_{ij}\delta_{kl} + D_2 \delta_{ik}\delta_{jl} + D_3 \delta_{il}\delta_{jk}, \tag{A.2}$$

where δ_{ij} is the Kronecker delta. Thus, we can obtain

$$A_{ijkl}^{iso} = \lambda \delta_{ij}\delta_{kl} + (G + \kappa)\,\delta_{ik}\delta_{jl} + (G - \kappa)\,\delta_{il}\delta_{jk},$$
$$B_{ijkl}^{iso} = B_1 \delta_{ij}\delta_{kl} + B_2 \delta_{jl} + B_3 \delta_{il}\delta_{jk},$$
$$C_{ijkl}^{iso} = \alpha \delta_{ij}\delta_{kl} + (\beta + \gamma)\,\delta_{ik}\delta_{jl} + (\beta - \gamma)\,\delta_{il}\delta_{jk}, \tag{A.3}$$

where λ and G are the Lamé constants, α, β, γ and κ are micropolar elastic constants, and B_1, B_2 and B_3 are elastic constants associated with chirality (noncentrosymmetry). For the cubical part, $A_{ijkl}^{cubic}, B_{ijkl}^{cubic}, C_{ijkl}^{cubic}$ can be written in a matrix form as

$$
A_{ijkl}^{cubic} = \begin{bmatrix} A_1^c & & & \\ & A_2^c & & \\ & & A_2^c & \\ & & & A_2^c \end{bmatrix}, A_1^c
$$
$$
= \begin{bmatrix} 2C_a & -C_a & -C_a \\ -C_a & 2C_a & -C_a \\ -C_a & -C_a & 2C_a \end{bmatrix}, A_2^c
$$
$$
= \begin{bmatrix} -C_a & -C_a \\ -C_a & -C_a \end{bmatrix},
$$
$$
B_{ijkl}^{cubic} = \begin{bmatrix} B_1^c & & & \\ & B_2^c & & \\ & & B_2^c & \\ & & & B_2^c \end{bmatrix}, B_1^c
$$
$$
= \begin{bmatrix} 2C_b & -C_b & -C_b \\ -C_b & 2C_b & -C_b \\ -C_b & -C_b & 2C_b \end{bmatrix}, B_2^c
$$
$$
= \begin{bmatrix} -C_b & -C_b \\ -C_b & -C_b \end{bmatrix},
$$
$$
C_{ijkl}^{cubic} = \begin{bmatrix} C_1^c & & & \\ & C_2^c & & \\ & & C_2^c & \\ & & & C_2^c \end{bmatrix}, C_1^c
$$
$$
= \begin{bmatrix} 2C_c & -C_c & -C_c \\ -C_c & 2C_c & -C_c \\ -C_c & -C_c & 2C_c \end{bmatrix}, C_2^c
$$
$$
= \begin{bmatrix} -C_c & -C_c \\ -C_c & -C_c \end{bmatrix}, \tag{A.4}
$$

where C_a, C_b and C_c are elastic constants characterizing cubic symmetry.

As a result, 12 elastic constants λ, G, κ, C_a; B_1, B_2, B_3, C_b; and α, β, γ, C_c are included in the three elastic tensors for 3D chiral micropolar solid with cubic symmetry. If a, b and c vanish, Eq. (4) reduces to the constitutive equations without cubic symmetry; if B_1, B_2 and B_3 also vanish, the isotropic micropolar elasticity is recovered; if α, β, γ and κ also vanish, then the constitutive equations are the same as those of classical Cauchy continuum theory. Based on the energy equivalence principle, the 12 elastic tensors can be obtained by Eq. (5).

Appendix B.

B.1. Solution for articulated multi-link mechanism.

This subsection shows in detail the procedure for solving the displacement and rotation degrees of freedom of the rigid outer square frame referring to Fig. 2. Based on the principle that the relative positions of any two points of the rigid body do not change before and after the motion, the geometric constraints equations are listed as

$$
\left\{
\begin{array}{c}
\left(\widetilde{r_i^m} - r_i^m\right)/4 = u_i^0 \\[4pt]
\left(\widetilde{r_i^m} - o_i^m\right)^2 = L_s^m, L_s^m = \left(r_i^m - o_i^m\right)^2 \\[4pt]
\left(\widetilde{r_i^m} - \widetilde{r_i^n}\right)^2 = L_b^m, L_b^m = \left(r_i^m - r_i^n\right)^2, n = \left\{ \begin{array}{c} m+1, (m = 1, 2, 3) \\ m - 3, (m = 4) \end{array} \right\} \\[8pt]
D_i \widetilde{r_i^4} + D_0 = 0, \left(O\widetilde{R^3} - O\widetilde{R^2} \quad and \quad O\widetilde{R^2} - O\widetilde{R^1} \quad construct \quad plane \quad D_1 x + D_2 y + D_3 z + D_0 = 0 \right)
\end{array}
\right\} \tag{B.1}
$$

Where $\boldsymbol{u^0} = \left(u_1^0, u_2^0, u_3^0\right)$ is a displacement constraint on the center of the rigid body $R^0\left(r_1^0, r_2^0, r_3^0\right)$, and $R^m\left(r_1^m, r_2^m, r_3^m\right)$ and $\widetilde{R^m}\left(\widetilde{r_1^m}, \widetilde{r_2^m}, \widetilde{r_3^m}\right)$ ($m = 1, 2, 3, 4$) are the position vectors of the vertices in the Cartesian coordinate system before and after the motion, respectively. This forms a system of homogeneous equations with twelve unknowns, and therefore leads to a unique non-zero solution.

The obtained position vectors of the vertices are utilized to derive the rotational degrees of freedom as
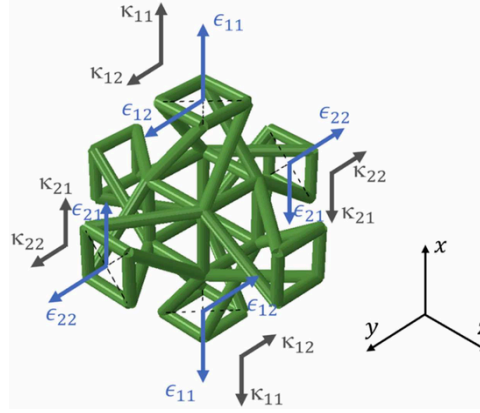
Fig. B.1. Boundary conditions of chiral unit cell.

Table B.1
Twelve boundary conditions sets and the corresponding strain energy of the chiral unit cell.

$Test_i$	States of ϵ_{ij} and κ_{ij}								w_i
	ϵ_{11}	ϵ_{22}	ϵ_{12}	ϵ_{21}	κ_{11}	κ_{22}	κ_{12}	κ_{21}	
1	ϵ^*	0	0	0	0	0	0	0	$w_1 = \epsilon^*\kappa^*(\lambda/2 + \mu + c)$
2	ϵ^*	ϵ^*	0	0	0	0	0	0	$w_2 = \epsilon^*\kappa^*(2\lambda + 2\mu + c)$
3	0	0	ϵ^*	0	0	0	0	0	$w_3 = \epsilon^*\kappa^*(\mu/2 + \kappa/4 - c/2)$
4	0	0	ϵ^*	ϵ^*	0	0	0	0	$w_4 = \epsilon^*\kappa^*(2\mu - 2c)$
5	ϵ^*	0	0	0	κ^*	0	0	0	$w_5 = \epsilon^*\kappa^*(\lambda/2 + \mu + B_1 + B_2 + B_3 + \alpha/2 + \beta/2$ $+ \gamma/2 + 2b + c + d)$
6	ϵ^*	ϵ^*	0	0	κ^*	κ^*	0	0	$w_6 = \epsilon^*\kappa^*(2\lambda + 2\mu + 4B_1 + 2B_2 + 2B_3 + 2\alpha + \beta + \gamma$ $+ 2b + c + d)$
7	0	0	ϵ^*	0	0	0	κ^*	0	$w_7 = \epsilon^*\kappa^*(\mu/2 + \kappa/4 + B_2 + \beta/2 - b - c/2 - d/2)$
8	0	0	ϵ^*	ϵ^*	0	0	κ^*	κ^*	$w_8 = \epsilon^*\kappa^*(2\mu + 2B_2 + 2B_3 + \beta + \gamma - 4b - 2c - 2d)$
9	0	0	0	0	κ^*	0	0	0	$w_9 = \epsilon^*\kappa^*(\alpha/2 + \beta/2 + \gamma/2 + d)$
10	0	0	0	0	κ^*	κ^*	0	0	$w_{10} = \epsilon^*\kappa^*(2\alpha + \beta + \gamma + d)$
11	0	0	0	0	0	0	κ^*	0	$w_{11} = \epsilon^*\kappa^*(\beta/2 - d/2)$
12	0	0	0	0	0	0	κ^*	κ^*	$w_{12} = \epsilon^*\kappa^*(\beta + \gamma - 2d)$

In this table, ε^* and k^* are predetermined strain and curvature respectively, and $w_i(i = 1, 2, \ldots, 12)$ is strain energy density calculated in 12 cases. And it should be noted that only x and y directions are activated doesn't lose generality because of cubic symmetry. Periodic boundary conditions are considered, and nonlinear geometry is on. Thus, the linear homogeneous equations of strain energy density are constructed, constituting a set of solutions for given geometry parameters.

$$\phi^0\left(\phi_1^0, \phi_2^0, \phi_3^0\right) = \cos^{-1}\left[\left(\widetilde{OR^m} - OR^0\right)\left(OR^m - OR^0\right)\right] \tag{B.2}$$

On the contrary, the translational displacements can also be derived by given rotational boundary constraint. Thus, the rotational and translational displacements of the rods under certain boundary condition are decoupled.

Transformation matrix is defined as

$$\lambda_0 = \begin{bmatrix} \lambda_{01} & 0 \\ 0 & \lambda_{01} \end{bmatrix} \tag{B.3}$$

In the matrix,

$$\lambda_{01} = \begin{bmatrix} l_{x\bar{x}} & l_{x\bar{y}} & l_{x\bar{z}} \\ l_{y\bar{x}} & l_{y\bar{y}} & l_{y\bar{z}} \\ l_{z\bar{x}} & l_{z\bar{y}} & l_{z\bar{z}} \end{bmatrix}$$

where $l_{x\bar{x}}, l_{x\bar{y}}, l_{x\bar{z}}$ is the cosine of the local coordinate x to the global coordinates $\bar{x}, \bar{y}, \bar{z}$ in three directions respectively, as

$$l_{x\bar{x}} = \cos(x, \bar{x}), \quad l_{x\bar{y}} = \cos(x, \bar{y}), \quad l_{x\bar{z}} = \cos(x, \bar{z}) \tag{B.4}$$

and $l_{y\bar{x}}, l_{y\bar{y}}, \ldots, l_{z\bar{z}}$ is the cosine of the local coordinate y and z to the global coordinates respectively.

B.2. FEM of the chiral unit cell

The FEM is analyzed by Abaqus Standard solver, where all rods of the chiral unit cell (Fig. 1b) are set as B31 beam elements with fine mesh. In order to obtain the numerical solution of the elasticity constants [30], twelve boundary conditions are set for the strain energy simulation of the chiral unit cell, as illustrated in Fig. B.1 and Table B.1.

See Appendix Fig. B.1 and Table B.1.

References

[1] X. Zheng, H. Lee, T.H. Weisgraber, M. Shusteff, J. Deotte, E.B. Duoss, J.D. Kuntz, M.M. Biener, Q. Ge, J.A. Jackson, S.O. Kucheyev, N.X. Fang, C.M. Spadaccini, Ultralight, ultrastiff mechanical metamaterials, Science 344 (2014) 1373–1377, https://doi.org/10.1126/science.1252291.

[2] J. Bauer, A. Schroer, R. Schwaiger, O. Kraft, Approaching theoretical strength in glassy carbon nanolattices, Nat. Mater. 15 (2016) 438–443, https://doi.org/10.1038/nmat4561.

[3] L.R. Meza, S. Das, J.R. Greer, Strong, lightweight, and recoverable three-dimensional ceramic nanolattices, Science 345 (2014) 1322–1326, https://doi.org/10.1126/science.1255908.

[4] C.S. Ha, R.S. Lakes, M.E. Plesha, Cubic negative stiffness lattice structure for energy absorption: numerical and experimental studies, Int. J. Solids Struct. 178–179 (2019) 127–135, https://doi.org/10.1016/j.ijsolstr.2019.06.024.

[5] T. Frenzel, C. Findeisen, M. Kadic, P. Gumbsch, M. Wegener, Tailored buckling microlattices as reusable light-weight shock absorbers, Adv. Mater. 28 (2016) 5865–5870, https://doi.org/10.1002/adma.201600610.

[6] J.L. Silverberg, J.-H. Na, A.A. Evans, B. Liu, T.C. Hull, Christian, R.J. Lang, R.C. Hayward, I. Cohen, Origami structures with a critical transition to bistability arising from hidden degrees of freedom, Nat. Mater. 14 (2015) 389–393, https://doi.org/10.1038/nmat4232.

[7] H.Y. Jeong, S.-C. An, I.C. Seo, E. Lee, S. Ha, N. Kim, Y.C. Jun, 3D printing of twisting and rotational bistable structures with tuning elements, Sci. Rep. (2019) 9, https://doi.org/10.1038/s41598-018-36936-6.

[8] S. Babaee, J. Shim, J.C. Weaver, E.R. Chen, N. Patel, K. Bertoldi, 3D soft metamaterials with negative poisson's ratio, Adv. Mater. 25 (2013) 5044–5049, https://doi.org/10.1002/adma.201301986.

[9] P. Vogiatzis, S. Chen, X. Wang, T. Li, L. Wang, Topology optimization of multi-material negative Poisson's ratio metamaterials using a reconciled level set method, Comput. Aided Des. 83 (2017) 15–32, https://doi.org/10.1016/j.cad.2016.09.009.

[10] X. Li, Z. Yang, Z. Lu, Design 3D metamaterials with compression-induced-twisting characteristics using shear–compression coupling effects, Extrem. Mech. Lett. 29 (2019) 100471, https://doi.org/10.1016/j.eml.2019.100471.

[11] J.I. Lipton, R. Maccurdy, Z. Manchester, L. Chin, D. Cellucci, D. Rus, Handedness in shearing auxetics creates rigid and compliant structures, Science 360 (2018) 632–635, https://doi.org/10.1126/science.aar4586.

[12] J.T.B. Overvelde, T.A. De Jong, Y. Shevchenko, S.A. Becerra, G.M. Whitesides, J.C. Weaver, C. Hoberman, K. Bertoldi, A three-dimensional actuated origami-inspired transformable metamaterial with multiple degrees of freedom, Nat. Commun. 7 (2016) 10929, https://doi.org/10.1038/ncomms10929.

[13] J.L. Silverberg, A.A. Evans, L. Mcleod, R.C. Hayward, T. Hull, C.D. Santangelo, I. Cohen, Using origami design principles to fold reprogrammable mechanical metamaterials, Science 345 (2014) 647–650, https://doi.org/10.1126/science.1252876.

[14] T. Bückmann, M. Thiel, M. Kadic, R. Schittny, M. Wegener, An elasto-mechanical unfeasibility cloak made of pentamode metamaterials, Nat. Commun. (2014) 5, https://doi.org/10.1038/ncomms5130.

[15] C. Coulais, A. Sabbadini, F. Vink, M. Van Hecke, Multi-step self-guided pathways for shape-changing metamaterials, Nature 561 (2018) 512–515, https://doi.org/10.1038/s41586-018-0541-0.

[16] X. Liu, G. Hu, Elastic metamaterials making use of chirality: a review, Stroj. Vestn. J. Mech. Eng. 62 (2016) 403–418, https://doi.org/10.5545/sv-jme.2016.3799.

[17] W. Wu, W. Hu, G. Qian, H. Liao, X. Xu, F. Berto, Mechanical design and multifunctional applications of chiral mechanical metamaterials: a review, Mater. Des. 180 (2019) 107950, https://doi.org/10.1016/j.matdes.2019.107950.

[18] B.K. Thomson, B. Kelvin, W. Thomson, Baltimore lectures on molecular dynamics and the wave theory of light, Cambridge University Press, 1904.

[19] D. Prall, R.S. Lakes, Properties of a chiral honeycomb with a poisson's ratio of -1, Int. J. Mech. Sci. 39 (1997) 305–314, https://doi.org/10.1016/s0020-7403(96)00025-2.

[20] X.N. Liu, G.L. Huang, G.K. Hu, Chiral effect in plane isotropic micropolar elasticity and its application to chiral lattices, J. Mech. Phys. Solids 60 (2012) 1907–1921, https://doi.org/10.1016/j.jmps.2012.06.008.

[21] C.S. Ha, M.E. Plesha, R.S. Lakes, Chiral three-dimensional isotropic lattices with negative Poisson's ratio, Phys. Status Solidi (b) 253 (2016) 1243–1251, https://doi.org/10.1002/pssb.201600055.

[22] H. Zong, H. Zhang, Y. Wang, M.Y. Wang, J.Y.H. Fuh, On two-step design of microstructure with desired Poisson's ratio for AM, Mater. Des. 159 (2018) 90–102, https://doi.org/10.1016/j.matdes.2018.08.032.

[23] P. Bettini, A. Airoldi, G. Sala, L.D. Landro, M. Ruzzene, A. Spadoni, Composite chiral structures for morphing airfoils: numerical analyses and development of a manufacturing process, Compos. Part B Eng. 41 (2010) 133–147, https://doi.org/10.1016/j.compositesb.2009.10.005.

[24] S.K. Bhullar, Influence of negative Poisson's ratio on stent applications, Adv. Mater. 2 (2013) 42, https://doi.org/10.11648/j.am.20130203.14.

[25] L.-C. Wang, W.-L. Song, D. Fang, Twistable origami and kirigami: from structure-guided smartness to mechanical energy storage, ACS Appl. Mater. Interfaces 11 (2019) 3450–3458, https://doi.org/10.1021/acsami.8b17776.

[26] Cosserat, E. and Cosserat, F., 1909. Theorie des corps déformables. A. Hermann et fils.

[27] A.C. Eringen, Microcontinuum field theories: I. Foundations and solids. & Business Media, Springer Science, 1999.

[28] T. Frenzel, M. Kadic, M. Wegener, Three-dimensional mechanical metamaterials with a twist, Science 358 (2017) 1072–1074, https://doi.org/10.1126/science.aao4640.

[29] M. Kadic, A. Diatta, T. Frenzel, S. Guenneau, M. Wegener, Static chiral Willis continuum mechanics for three-dimensional chiral mechanical metamaterials, Phys. Rev. B (2019) 99, https://doi.org/10.1103/physrevb.99.214101.

[30] S. Duan, W. Wen, D. Fang, A predictive micropolar continuum model for a novel three-dimensional chiral lattice with size effect and tension-twist coupling behavior, J. Mech. Phys. Solids 121 (2018) 23–46, https://doi.org/10.1016/j.jmps.2018.07.016.

[31] W. Wu, L. Geng, Y. Niu, D. Qi, X. Cui, D. Fang, Compression twist deformation of novel tetrachiral architected cylindrical tube inspired by towel gourd tendrils, Extrem. Mech. Lett. 20 (2018) 104–111, https://doi.org/10.1016/j.eml.2018.02.001.

[32] P. Ziemke, T. Frenzel, M. Wegener, P. Gumbsch, Tailoring the characteristic length scale of 3D chiral mechanical metamaterials, Extrem. Mech. Lett. 32 (2019) 100553, https://doi.org/10.1016/j.eml.2019.100553.

[33] W. Chen, X. Huang, Topological design of 3D chiral metamaterials based on couple-stress homogenization, J. Mech. Phys. Solids 131 (2019) 372–386, https://doi.org/10.1016/j.jmps.2019.07.014.

[34] C. Ma, H. Lei, J. Liang, W. Wu, T. Wang, D. Fang, Macroscopic mechanical response of chiral-type cylindrical metastructures under axial compression loading, Mater. Des. 158 (2018) 198–212, https://doi.org/10.1016/j.matdes.2018.08.022.

[35] C.S. Ha, M.E. Plesha, R.S. Lakes, Chiral three-dimensional lattices with tunable Poisson's ratio, Smart Mater. Struct. 25 (2016) 054005, https://doi.org/10.1088/0964-1726/25/5/054005.

[36] W. Zhang, X.Y. Bai, B.W. Hou, Y.D. Sun, X. Han, Mechanical properties of the three-dimensional compression-twist cellular structure, J. Reinf. Plast. Compos. 39 (2019) 260–277, https://doi.org/10.1177/0731684419888588.

[37] H.-H. Huang, B.-L. Wong, Y.-C. Chou, Design and properties of 3D-printed chiral auxetic metamaterials by reconfigurable connections, Phys. Status Solidi (b) 253 (2016) 1557–1564, https://doi.org/10.1002/pssb.201600027.

[38] R.S. Lakes, R.L. Benedict, Noncentrosymmetry in micropolar elasticity, Int. J. Eng. Sci. 20 (1982) 1161–1167, https://doi.org/10.1016/0020-7225(82)90096-9.

[39] Y. Liu, P. Ben-Tzvi, Design, analysis, and integration of a new two-degree-of-freedom articulated multi-link robotic tail mechanism, J. Mech. Robot. 12 (2020) 1–30, https://doi.org/10.1115/1.4045842.

[40] Kakogawa, A., Oka, Y., Ma, S., 2018. Multi-link Articulated Wheeled In-pipe Robot with Underactuated Twisting Joints, in: doi:10.1109/icma.2018.8484370.

[41] R.S. Lakes, Size effects and micromechanics of a porous solid, J. Mater. Sci. 18 (1983) 2572–2580, https://doi.org/10.1007/bf00547573.

[42] J.F. Yang, R.S. Lakes, Experimental study of micropolar and couple stress elasticity in compact bone in bending, J. Biomech. 15 (1983) 91–98, https://doi.org/10.1016/0021-9290(82)90040-9.

[43] W.N. Zou, Q.S. Zheng, D.X. Du, J. Rychlewski, Orthogonal irreducible decompositions of tensors of high orders, Math. Mech. Solids 6 (2001) 249–267, 0.1177/108128650100600303.